16èmes Journées de l'Hydrodynamique
27-29 novembre 2018 - Marseille

PHASE-RESOLVED PREDICTION OF NONLINEAR OCEAN WAVE FIELDS FROM REMOTE OPTICAL MEASUREMENTS

PRÉDICTION À PHASE RÉSOLUE DE CHAMP DE VAGUES NON-LINÉAIRE PAR TÉLÉDÉTECTION OPTIQUE

N. DESMARS[(1)]*, Y. PERIGNON[(1)], G. DUCROZET[(1)], C.-A. GUÉRIN[(2)], S. T. GRILLI[(3)], P. FERRANT[(1)]

[(1)]LHEEA Lab, UMR CNRS 6598, École Centrale de Nantes
[(2)]Mediterranean Institute of Oceanography (MIO UM 110), IRD, CNRS-INSU, Université de Toulon
[(3)]Department of Ocean Engineering, University of Rhode Island, USA

Summary

The performance of a phase-resolved algorithm is assessed for the prediction of nonlinear ocean wave fields based on remote optical measurements of free surface elevations in space and time. The accuracy of the wave forecast is evaluated here for the simple case of a unidirectional wave field, by ensemble averaging a large number of synthetic data sets. For several characteristic wave steepnesses, we compare results based on linear wave theory and a new weakly nonlinear Lagrangian wave model. Results show that the proposed nonlinear model is able to simulate relevant nonlinear effects that play an increasingly large role as wave steepness becomes larger, such as wave shape asymmetry and phase shift. Experimental data is also used to illustrate the performance of the method for actual wave field measurements.

Résumé

Les performances d'une méthode de prédiction de champs de vagues non-linéaires à partir de mesures optiques spatio-temporelles d'élévation de surface sont étudiées. Afin de quantifier la qualité des prédictions, des indicateurs d'erreur sont estimés dans le cas d'une houle unidirectionnelle en moyennant les résultats sur un grand nombre de données synthétiques. Pour quelques cambrures caractéristiques, nous comparons les résultats issus d'approches linéaire et faiblement non-linéaire. Il est montré que le modèle non-linéaire utilisé, basé sur une description Lagrangienne de la dynamique de surface libre, permet de capter des effets non-linéaires jouant un rôle important et grandissant avec la cambrure, en particulier l'asymétrie de forme et le déphasage. Des données expérimentales sont également utilisées pour illustrer les performances de la méthode appliquée à des mesures réelles.

*Corresponding author. E-mail address: nicolas.desmars@ec-nantes.fr

I – Introduction: Formulation of the Prediction Problem

To many offshore applications, such as the optimal maneuvering and operational guidance of surface vessels or active control of ocean renewable energy harvesting systems, the capacity to predict in real-time the incoming phase-resolved wave field is a crucial issue. This problem was studied in some earlier work on the basis of free surface elevation time series measured at fixed wave probes [1, 23, 24]. However, in situ measurements, typically made from a moving vessel or vehicle, are more challenging since wave reconstruction must rely on data acquired at constantly updated locations surrounding the path of the vehicle, which leads to practical limitations. Solutions to this problem is proposed based on X-band radar measurements made from an on-board sensor, combined with a 3D-FT to reconstruct a large patch of free surface elevation surrounding the sensor [4, 12, 13, 22, 26]. This initial estimate is then used in a direct numerical simulation of the future evolution of the sea state.

Here, we present recent developments of a method for reconstructing and predicting ocean waves in the short term, ahead of a moving or fixed ocean structure, based on optical measurements such as made with a LIDAR camera mounted on the structure.

The general wave prediction problem is formulated in the form of explicit relationships between the main parameters of the problem, i.e., the incoming wave field, the targeted prediction horizon (time span during which the wave field dynamics can be estimated), and the kinematics and size of the structure of interest (e.g., a moving ship, a marine energy device).

Since typical wave fields are bounded in frequency and direction of propagation (i.e., the energy is not homogeneously spread out over all frequencies/directions), a basic statistical knowledge of the incoming sea state can help to define relevant bandwidths for accurately representing the underlying deterministic fields. In the following, the wave field directional energy density spectrum $S(k, \theta)$ is assumed to be known, where $k(\omega)$ is the frequency-dependent wavenumber, with ω and θ the wave angular frequency and direction of propagation, respectively. The prediction horizon corresponds to the time constraint of the prediction problem, i.e., the time needed for the structure control system or operator to adequately react to changes in incoming waves. The ocean structure motion defines its path (assumed to be known), which together with the structure size allows calculating the spatio-temporal area over which wave dynamics is to be predicted.

A central element in the wave prediction problem, relating the aforementioned parameters, is the concept of accessible prediction zone, that is the spatial area denoted here by $\mathcal{P}(t)$, over which sufficient information on the wave field is available to adequately predict its dynamics. This is detailed in the next section.

Accordingly, the wave prediction problem is formulated as follows: based on adequately located real-time ocean surface measurements, extract and process sufficient data to predict the wave dynamics at the structure's future position, fast enough to satisfy the prediction horizon constraint.

II – Application to Optical Measurements

II – 1 Accessible Prediction Zone from Nonuniform Observations

Earlier work has shown that the spatio-temporal region over which wave dynamics can be predicted based on a set of free surface measurements, is bounded [14, 21, 25]. When measurements are made using an optical system, at a specific sampling rate and over a given observation zone, this limits the amount of data that can be assimilated and used in the wave reconstruction process, yielding a reconstructed surface in space/time defined with finite frequency and direction bandwidths. In light of this, the sea-state prediction obtained by propagating the assimilated information is similarly limited to a spatio-temporal region referred to as prediction zone. In the following, we show how the latter can be defined for a set of nonuniform observations made in a unidirectional wave field (i.e., irregularly distributed in space).

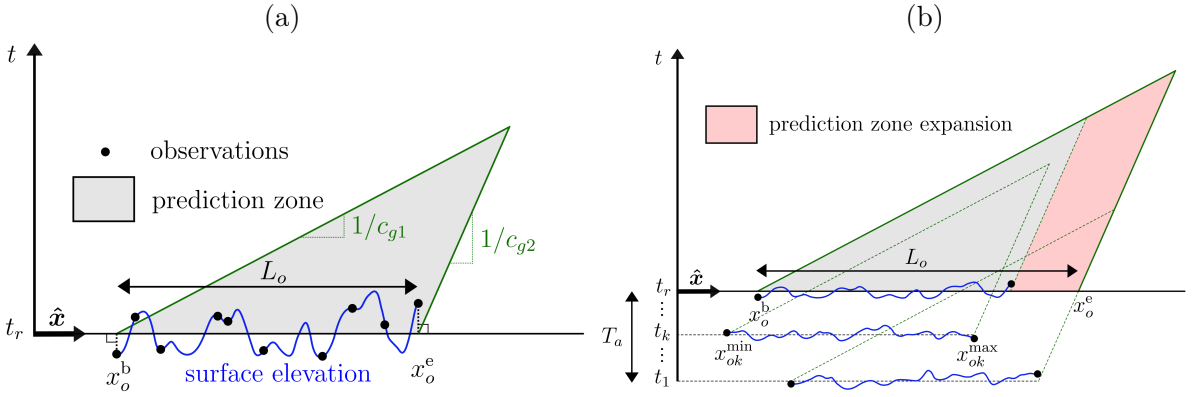

Figure 1: Evolution of the prediction zone in time and space, for: (a) spatial data; and (b) spatio-temporal data (dash lines are prediction zones boundaries at time t_k; the increase in prediction zone relative to that of spatial observations is highlighted in red.

Both theoretical and experimental studies have shown that directional components in a dispersive wave field, of given amplitude, frequency, and phase, travel at the associated group velocity along their direction of propagation [14, 21]. The intersections of the slowest and fastest components thus determine the boundary of the spatio-temporal region over which information is available and a prediction can be issued. Consequently, as time increases, the accessible prediction zone shrinks, to eventually disappear when the assimilated information is completely dispersed in space. Figure 1 illustrates this phenomenon for a unidirectional wave field propagating in the x-direction. The last time used for the assimilation corresponds to the reconstruction time t_r. If only spatial data is used in the assimilation (Fig. 1a), the prediction zone at reconstruction time $\mathcal{P}(t_r)$ is the spatial area where observations were made. However, when spatio-temporal data sets are used (over an assimilation time T_a; Fig. 1b), $\mathcal{P}(t_r)$ expands due to the advection of wave information during T_a. A point $(x, t \geq t_r)$ is included in the prediction zone if,

$$x_o^{\mathrm{b}} + c_{g1}(t - t_r) \leq x \leq x_o^{\mathrm{e}} + c_{g2}(t - t_r), \tag{1}$$

where c_{g1} and c_{g2} are the fastest and slowest group velocities, respectively, and x_o^{b} and x_o^{e} define the beginning and the end of $\mathcal{P}(t_r)$ as,

$$\begin{cases} x_o^{\mathrm{b}} = \min\limits_k \left\{ x_{ok}^{\min} + c_{g1}(t_r - t_k) \right\}, \\ x_o^{\mathrm{e}} = \max\limits_k \left\{ x_{ok}^{\max} + c_{g2}(t_r - t_k) \right\}, \end{cases} \tag{2}$$

where index $k \in \{1, ..., K\}$ with K the number of observation times.

II – 2 Bandwidths of the Reconstructed Wave Field

The dynamics of a wave field is governed by the propagation of its most energetic components. Since ocean wave generation processes eventually yield energy spectra with fairly narrow frequency bandwidth in their main direction of propagation, the dynamics of the wave field can be accurately represented by finite frequency and direction bandwidths having appropriate cutoff limits $\left(k^{\min,\max}, \theta^{\min,\max}\right)$.

As mentioned above, the spatio-temporal characteristics of the observation grid constrain the wave information that is accessible. The smallest wavenumber measurable in this grid $k^{\min} = 2\pi/L_o$ is function of the largest distance $L_o = x_o^{\mathrm{e}} - x_o^{\mathrm{b}}$ between two observation points at reconstruction time t_r (see Fig. 1b). However, L_o itself depends on the minimum and maximum group velocities, thus on the cutoff frequencies. This paradox is resolved by conservatively calculating $k^{\min} = 2\pi/L_c$, with $L_c = x_o^{\mathrm{e}} - x_{o(k=K)}^{\min} \leq L_o$. L_c only depends on the spatio-temporal location of the observations and on the minimum group velocity, which is related to the high

cutoff wavenumber $k^{\max}$. When reconstructing a signal over a regular observation grid (i.e., with a constant spatial sampling), the maximum high cutoff frequency must satisfy Shannon's condition $k^{\max} \leq 2\pi/(2\ell_o)$ where ℓ_o is the distance between two observation points. Since the observation grid is highly irregular when using an optical method [16], $k^{\max}$ is set so that the spectral energy truncated at higher frequencies is negligible for the dynamic description of the wave field. Also, since optical measurements provide observations at many spatial locations, there is no constraints on the cutoff directions from the observation grid. Hence, likewise $k^{\max}$, $\theta^{\min,\max}$ are calculated based on the truncation of a negligible amount of energy. If an estimate of the underlying wave field is known, one way to choose these parameters is to evaluate their influence on the quality of the reconstructed or predicted wave fields, since a convergence of the quality of the reconstruction/prediction is expected as $k^{\max}$ increases and $\left[\theta^{\min}, \theta^{\max}\right]$ gets larger. In operational conditions, such information is not typically available and one must rely on an estimate of the wave spectrum, for instance based on measurements of the motion of the structure of interest, or from earlier measurements of free surface elevations. In this case, relevant values of $k^{\max}$ and $\theta^{\min,\max}$ can be selected by ensuring that,

$$\int_{k^{\min}}^{k^{\max}} \int_{\theta^{\min}}^{\theta^{\max}} S(k,\theta)\,\mathrm{d}\theta\,\mathrm{d}k \leq (1-\mu) \int_0^{+\infty} \int_0^{2\pi} S(k,\theta)\,\mathrm{d}\theta\,\mathrm{d}k, \tag{3}$$

where $S(k,\theta)$ is the directional wave energy density spectrum and $\mu \ll 1$ is the fraction of total energy that can be considered as negligible on free surface dynamics.

II – 3 Group Velocities for the Determination of the Prediction Zone

In practice, the cutoff frequencies calculated for the wave field reconstruction can be too restrictive for the determination of the evolution of the prediction zone. Hence, the wave group velocities $c_{g1,2}$ that govern the evolution of the prediction zone boundaries are instead defined based on two wavenumbers $k_{1,2}$, such that,

$$F(k_1) = F(k_2) = \mu F(k_p), \tag{4}$$

where $F(k) = \int_0^{2\pi} S(k,\theta)\,\mathrm{d}\theta$ is the one-sided wave spectrum, k_p is the wavenumber based on its peak wavelength, i.e., that of maximum energy, and μ is a small fraction, here, of the peak spectral energy. k_1 (k_2) is the smallest (largest) wavenumber to respect condition (4). In the following, we will use the linear deep water dispersion relationship to estimate the group velocities from $k_{1,2}$.

III – Wave Models

Computing real-time wave predictions using complex, highly nonlinear, wave models, such as based on High-Order Spectral method, is challenging and may lead to prohibitive computing times. Hence, similar to earlier work [16], we seek to apply a model that properly accounts for nonlinear effects, which may significantly affect wave propagation in strong sea-states, while being suitable for the real-time constraint of the prediction problem. In this work, we consider and compare two wave models: a simple model based on linear wave theory (LWT), and a weakly nonlinear wave model, denoted as *Improved Choppy Wave Model* (ICWM) [10], derived from a Lagrangian approach of the description of the fluid motion, as an improved version of the earlier CWM [17,18]. When applied to a set of observations, both models provide an analytic expression of the reconstructed free surface elevations, which allows for a very efficient numerical prediction of wave propagation, by simply increasing time in the formulation.

III – 1 Linear Wave Theory

Linear Wave Theory (LWT) refers to the Stokes wave model derived based on the classical Eulerian approach and linearized with respect to wave steepness. With this model, the ocean

surface is represented in a Cartesian coordinate system (x, y, z) (with x and y axes located on the mean water surface and the z-axis being vertical and positive upward) as the superposition of N individual periodic waves of amplitudes A_n, wavelengths λ_n, and propagating in directions θ_n with respect to the x-axis, as,

$$\eta(\boldsymbol{r}, t) = \sum_{n=1}^{N} A_n \cos\left(\boldsymbol{k}_n \cdot \boldsymbol{r} - \omega_n t + \varphi_n\right), \tag{5}$$

with $\boldsymbol{r} = (x, y)$ the horizontal position vector, t the time, φ_n a set of random phases uniformly distributed in $[0, 2\pi]$, and $\boldsymbol{k}_n = k_n \hat{\boldsymbol{k}}_n = (k_n \cos\theta_n, k_n \sin\theta_n)$ the wavenumber vectors, with $k_n = 2\pi/\lambda_n$. The latter are related to angular frequencies ω_n through the deep water linear dispersion relationship.

To simplify the mathematical formalism of wave field reconstruction methods developed hereafter, Eq. (5) is recast as,

$$\eta(\boldsymbol{r}, t) = \sum_{n=1}^{N} a_n \cos\psi_n + b_n \sin\psi_n, \tag{6}$$

where $\psi_n = \boldsymbol{k}_n \cdot \boldsymbol{r} - \omega_n t$ are spatio-temporal phases, and $(a_n, b_n) = (A_n \cos\varphi_n, A_n \sin\varphi_n)$ are wave parameters describing the ocean surface.

III – 2 Improved Choppy Wave Model

At each data acquisition time, optical measurements of ocean waves provide surface elevations measured at a set of irregularly distributed points of known coordinates in the reference frame. Earlier ocean surface reconstruction and prediction algorithms were implemented to use such irregular data sets [16, 25]. Moreover, Nouguier et al's [16] algorithm, which is extended here, was based on the Lagrangian CWM [8, 17, 18], which can simulate higher-order nonlinear wave properties, in terms of steepness, than Eulerian models of the same order. In the following the CWM equations are recast as the solution of Lagrangian dynamical equations in an Eulerian system.

Considering a water particle located on the ocean surface at coordinates $\boldsymbol{\xi}$ in the horizontal plane, its horizontal and vertical displacements are found as a Lagrangian perturbation expansion in wave steepness as [15, 19, 20],

$$\begin{cases} \boldsymbol{r}(\boldsymbol{\xi}, t) = \boldsymbol{\xi} + \sum_i \boldsymbol{D}_i(\boldsymbol{\xi}, t), \\ z(\boldsymbol{\xi}, t) = \sum_i Z_i(\boldsymbol{\xi}, t), \end{cases} \tag{7}$$

respectively, where $\boldsymbol{D}_i$ and Z_i are the horizontal and vertical particle displacements with respect to the particle position at rest $\boldsymbol{\xi}$ associated with the i^{th}-order of expansion, respectively. Noting an inconsistency in the Stokes drift predicted by the CWM, Guérin et al. [10] added a correction to these equations, yielding the Improved Choppy Wave Model (ICWM),

$$\begin{cases} \boldsymbol{r}(\boldsymbol{\xi}, t) = \boldsymbol{\xi} + \sum_{n=1}^{N} \hat{\boldsymbol{k}}_n \left(-a_n \sin\tilde{\psi}_n + b_n \cos\tilde{\psi}_n\right) + \boldsymbol{\mathcal{U}}_s t, \\ z(\boldsymbol{\xi}, t) = \sum_{n=1}^{N} \left(a_n \cos\tilde{\psi}_n + b_n \sin\tilde{\psi}_n + \frac{1}{2}\left(a_n^2 + b_n^2\right) k_n\right), \end{cases} \tag{8}$$

where $\tilde{\psi}_n = \boldsymbol{k}_n \cdot \boldsymbol{r} - \tilde{\omega}_n t$, $\tilde{\omega}_n = \omega_n - 1/2 \boldsymbol{k}_n \cdot \boldsymbol{\mathcal{U}}_s$ and $\boldsymbol{\mathcal{U}}_s = \sum_{n=1}^{N} \left(a_n^2 + b_n^2\right) \omega_n \boldsymbol{k}_n$.

To use ICWM in practical simulations, its Lagrangian formulation Eq. (8) is first transformed into an equivalent Eulerian model, by deriving an approximate explicit relationship between $\boldsymbol{r}$ and z. First, the horizontal particle shift $\boldsymbol{\mathcal{U}}_s t$ is implicitly incorporated into a modified angular frequency, which yields,

$$\begin{cases} \boldsymbol{\mathcal{R}}(\boldsymbol{\xi}, t) = \boldsymbol{r}(\boldsymbol{\xi} - \boldsymbol{\mathcal{U}}_s t, t) = \boldsymbol{\xi} + \boldsymbol{\mathcal{D}}(\boldsymbol{\xi}) = \boldsymbol{\xi} + \sum_{n=1}^{N} \hat{\boldsymbol{k}}_n \left(-a_n \sin\psi_{\mathrm{L}n} + b_n \cos\psi_{\mathrm{L}n}\right), \\ \mathcal{Z}(\boldsymbol{\xi}, t) = z(\boldsymbol{\xi} - \boldsymbol{\mathcal{U}}_s t, t) = \sum_{n=1}^{N} \left(a_n \cos\psi_{\mathrm{L}n} + b_n \sin\psi_{\mathrm{L}n} + \frac{1}{2}\left(a_n^2 + b_n^2\right) k_n\right), \end{cases} \tag{9}$$

where $\psi_{\mathrm{L}n} = \boldsymbol{k}_n \cdot \boldsymbol{r} - \omega_{\mathrm{L}n} t$ and $\omega_{\mathrm{L}n} = \omega_n + 1/2 \boldsymbol{k}_n \cdot \boldsymbol{\mathcal{U}}_s$. Then, the particle horizontal displacement $\boldsymbol{\mathcal{D}}$ is calculated at the current particle location $\boldsymbol{\mathcal{R}}$ rather than at its reference location $\boldsymbol{\xi}$, as,

$$\mathcal{Z}(\boldsymbol{\xi}) = \mathcal{Z}(\boldsymbol{\mathcal{R}} - \boldsymbol{\mathcal{D}}(\boldsymbol{\xi})) \simeq \mathcal{Z}(\boldsymbol{\mathcal{R}} - \boldsymbol{\mathcal{D}}(\boldsymbol{\mathcal{R}})) = \tilde{\eta}(\boldsymbol{\mathcal{R}}). \tag{10}$$

Accordingly, the free surface elevation at any location $\boldsymbol{r}$ reads,

$$\tilde{\eta}(\boldsymbol{r}, t) = \sum_{n=1}^{N} \left(a_n \cos \Psi_n + b_n \sin \Psi_n + \frac{1}{2} \left(a_n^2 + b_n^2 \right) k_n \right), \quad \text{with,} \tag{11}$$

$$\Psi_n = \boldsymbol{k}_n \cdot \left(\boldsymbol{r} - \sum_{n=1}^{N} \hat{\boldsymbol{k}}_n \left(-a_n \sin \psi_{\mathrm{L}n} + b_n \cos \psi_{\mathrm{L}n} \right) \right) - \omega_{\mathrm{L}n} t.$$

Earlier work has shown [9, 16] that errors due to the approximation made in Eq. (10) are of the order of the mean square slope (i.e., the second-order moment of the one-sided wave spectrum $\int_0^{+\infty} k^2 F(k)\, \mathrm{d}k$) of the ocean surface, which is expected to be small compared to other sources of error in the reconstruction process.

III – 3 Ocean Surface Reconstruction

Similar to earlier work [9, 16], the ocean surface is reconstructed, using either LWT or ICWM, based on determining model parameters that minimize the mean square error between spatio-temporal ocean observations and their representation in the model, referred to as the *Cost Function*, i.e.,

$$C(\boldsymbol{p}) = \sum_{k=1}^{K} \sum_{j=1}^{J} \left(\eta_{jk}(\boldsymbol{p}) - \overline{\eta}_{jk} \right)^2 = \sum_{\ell=1}^{L} \left(\eta_\ell(\boldsymbol{p}) - \overline{\eta}_\ell \right)^2, \tag{12}$$

in which $\boldsymbol{p} = \{a_n, b_n\}$ ($n \in \{1, ..., N\}$) is the control vector containing the $2N$ unknown model parameters, J and K are the number of spatial observations made at each observation time and the number of observation times, respectively (hence, the total number of spatio-temporal observations assimilated in the model is, $J \times K = L$), $\overline{\eta}_{jk}$ are free surface elevations measured at spatial locations $\boldsymbol{r}_j$ ($j \in \{1, ..., J\}$) and times t_k ($k \in \{1, ..., K\}$), η_{jk} are estimates of these made using the wave model, i.e., with Eq. (6) for LWT or Eq. (11) for ICWM.

III – 3.1 Linear Wave Field

The ocean surface is reconstructed through a least square minimization of the cost function, as,

$$\left\{ \frac{\partial C}{\partial a_m} = 0, \quad \frac{\partial C}{\partial b_m} = 0 \right\} \iff \mathsf{A}_{mn} p_n = \mathsf{B}_m, \tag{13}$$

for $n, m \in \{1, ..., N\}$ (note that index summation is implied for repeated indices), with,

$$p_n = a_n, \quad p_{N+n} = b_n, \tag{14}$$

the control vector of $2N$ unknown wave parameters. According to LWT, the right hand side vector, which contains observations, reads,

$$\mathsf{B}_m = \sum_{\ell=1}^{L} \overline{\eta}_\ell \cos \psi_{m\ell}, \quad \mathsf{B}_{N+m} = \sum_{\ell=1}^{L} \overline{\eta}_\ell \sin \psi_{m\ell}, \tag{15}$$

and the $2N \times 2N$ matrix A_{mn} reads,

$$\begin{aligned}
\mathsf{A}_{mn} &= \sum_{\ell=1}^{L} \cos\psi_{n\ell}\cos\psi_{m\ell}, \qquad & \mathsf{A}_{m,N+n} &= \sum_{\ell=1}^{L} \sin\psi_{n\ell}\cos\psi_{m\ell}, \\
\mathsf{A}_{N+m,n} &= \sum_{\ell=1}^{L} \cos\psi_{n\ell}\sin\psi_{m\ell}, \qquad & \mathsf{A}_{N+m,N+n} &= \sum_{\ell=1}^{L} \sin\psi_{n\ell}\sin\psi_{m\ell}.
\end{aligned} \tag{16}$$

The linear system of Eqs. (13) is solved for the model parameters (a_n, b_n), with the relevant number of frequency components N being determined through a convergence study.

III – 3.2 Nonlinear Wave Field

Using the weakly nonlinear ICWM formulation (11), we have,

$$\mathsf{B}_m = \sum_{\ell=1}^{L} \overline{\eta}_\ell P_{m\ell}, \quad \mathsf{B}_{N+m} = \sum_{\ell=1}^{L} \overline{\eta}_\ell Q_{m\ell}, \tag{17}$$

and

$$\begin{aligned}
\mathsf{A}_{mn} &= \sum_{\ell=1}^{L} \left(\cos\Psi_{n\ell} + \frac{1}{2}a_n k_n\right) P_{m\ell}, \qquad & \mathsf{A}_{m,N+n} &= \sum_{\ell=1}^{L} \left(\sin\Psi_{n\ell} + \frac{1}{2}b_n k_n\right) P_{m\ell}, \\
\mathsf{A}_{N+m,n} &= \sum_{\ell=1}^{L} \left(\cos\Psi_{n\ell} + \frac{1}{2}a_n k_n\right) Q_{m\ell}, \qquad & \mathsf{A}_{N+m,N+n} &= \sum_{\ell=1}^{L} \left(\sin\Psi_{n\ell} + \frac{1}{2}b_n k_n\right) Q_{m\ell},
\end{aligned} \tag{18}$$

in which,

$$\begin{cases}
P_{m\ell} = \cos\Psi_{m\ell} - k_m\left(a_m\sin\Psi_{m\ell} - b_m\cos\Psi_{m\ell}\right)\times \\
\qquad\qquad \left\{\sin\psi_{\mathrm{L}m\ell} - \left[k_m\left(a_m\cos\psi_{\mathrm{L}m\ell} + b_m\sin\psi_{\mathrm{L}m\ell}\right) + 1\right] a_m\omega_m k_m t_\ell\right\} + a_m k_m, \\
Q_{m\ell} = \sin\Psi_{m\ell} - k_m\left(a_m\sin\Psi_{m\ell} - b_m\cos\Psi_{m\ell}\right)\times \\
\qquad\qquad \left\{-\cos\psi_{\mathrm{L}m\ell} - \left[k_m\left(a_m\cos\psi_{\mathrm{L}m\ell} + b_m\sin\psi_{\mathrm{L}m\ell}\right) + 1\right] b_m\omega_m k_m t_\ell\right\} + b_m k_m.
\end{cases} \tag{19}$$

Since both A_{mn} and B_m now depend on wave parameters (a_n, b_n), the system of equations (13) is solved iteratively [16]. Thus, when solving for $p_n^{(q+1)}$ at iteration $q+1$, $\mathsf{A}_{mn}^{(q)}$ and $\mathsf{B}_m^{(q)}$ are based on wave parameters obtained at the previous iteration q. The solution is initialized at $q = 0$ using $\mathsf{A}_{mn}^{(0)}$ and $\mathsf{B}_m^{(0)}$ computed for the linear reconstruction with Eqs. (15) and (16). Convergence is typically achieved within 5 to 20 iterations depending on wave steepness.

III – 3.3 Regularization of the Solution

In applications, the ocean reconstruction problem may become ill-conditioned due to practical constraints, such as the heterogeneous distribution of spatial observation points, the limited ocean area observed by the optical sensor, and the frequency and direction bandwidth cutoffs in the reconstructed wave field. Nevertheless, consistent results can be achieved, independently of the conditioning of the system matrix to invert (i.e., A_{mn}), through a Tikhonov regularization procedure, in which the matrix inversion is replaced by a minimization problem as,

$$\min\left\{||\mathsf{A}_{mn}p_n - \mathsf{B}_m||^2 - \mathsf{r}^2\,||p_n||^2\right\}, \tag{20}$$

where r is the regularization parameter. The optimal value of the regularization parameter is found using the "L-curve" method, which consists in finding the r value corresponding to the point

of maximal curvature (i.e., corner) of the function $(\log||\mathsf{A}_{mn}p_n - \mathsf{B}_m||, \log||p_n||)$. This method thus provides an optimal compromise between minimizing the residual error and ensuring that the norm of the solution does not become too large, i.e., ill-posed. The L-curve corner can be determined analytically through solving a singular value decomposition problem [3, 11]. Note that this procedure is equivalent to adding a constraint to the minimization problem, physically representing the total energy of the reconstructed wave spectrum, since the latter is proportional to the squared norm of p_n; in this case, $-\mathsf{r}^2$ can simply be interpreted as a Lagrangian multiplier.

IV – Synthetic Application Case

In this application, similar to [9, 16], one-dimensional synthetic optical data is geometrically created for irregular sea states described by their wave energy spectrum and generated using a nonlinear wave model, here the HOS-ocean model [2,6,7]. The ocean surface is then reconstructed and predicted based on this data set and compared to the original surface η_{HOS}. This is repeated for realistic sea states of various characteristic steepnesses. Sea state parameters and optical sensor configuration are similar to those used in earlier work [5], as briefly recapped below.

IV – 1 Setup and Error Definitions

A fixed optical sensor, located at abscissa x_c and elevation $z_c = 30$ m observes the ocean surface for $x < x_c$, with a mean viewing angle $\alpha = 76°$, an aperture angle $\alpha_a = 20°$, and along $J = 64$ rays, which are homogeneously distributed over the aperture angle (Fig. 2). The sea state

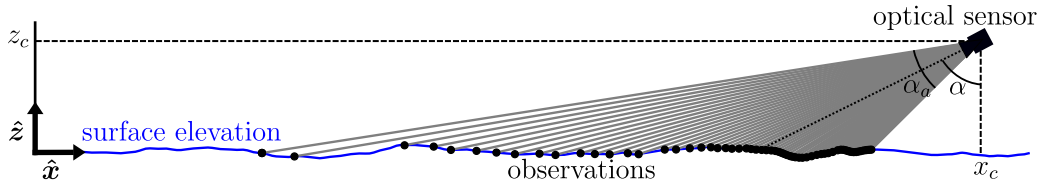

Figure 2: Setup for the spatial sampling of a unidirectional wave field.

is represented by a JONSWAP spectrum of peak period $T_p = 10$ s and peakedness $\gamma = 3.3$. The significant wave height H_s varies between 1.5 and 6 m. Converged results were achieved using $N = 50$ frequency components, a high cutoff wavenumber $k^{\max} = 10k_p$, and a number of observation times $K = 10$ with a sampling rate of 1 Hz. The spatio-temporal target zone for wave prediction $\mathcal{T}(t)$ is 100 m long, centered on the sensor location x_c, spans a 10 s time, from 20 to 30 s after the first waves enter the region. Hence, a point (x, t) is in the target zone if $x_c - 50 \leq x \leq x_c + 50$ and $t_r + 20 \leq t \leq t_r + 30$.

Two error indicators are used to quantify the prediction accuracy. The first one is a local "point to point" error,

$$\varepsilon(x,t) = |\eta(x,t) - \eta_{\mathrm{HOS}}(x,t)| / H_s. \tag{21}$$

In the second one, statistics are calculated by ensemble averaging 1,000 independent sea state realizations, generated for different sets of random phases. For each sea state, the average root mean square (RMS) error is calculated as,

$$\varepsilon_{\mathrm{RMS}}(t) = \left[\int_{\mathcal{T}(t)} (\eta(x,t) - \eta_{\mathrm{HOS}}(x,t))^2 \,\mathrm{d}x \Big/ \int_{\mathcal{T}(t)} \eta_{\mathrm{HOS}}^2 \,\mathrm{d}x \right]^{1/2}, \tag{22}$$

with η is the predicted elevation using LWT or ICWM. This error is finally averaged over the 1,000 realizations.

IV – 2 Results

The ocean surface predicted using the LWT or the ICWM models are compared with each other and with the reference solution based on the two previously defined error indicators.

Thus, Fig. 3a shows $\varepsilon(x,t)$ computed over a large spatio-temporal domain using ICWM, for a specific realization with $H_s = 3$ m. Boundaries of the prediction zone are calculated

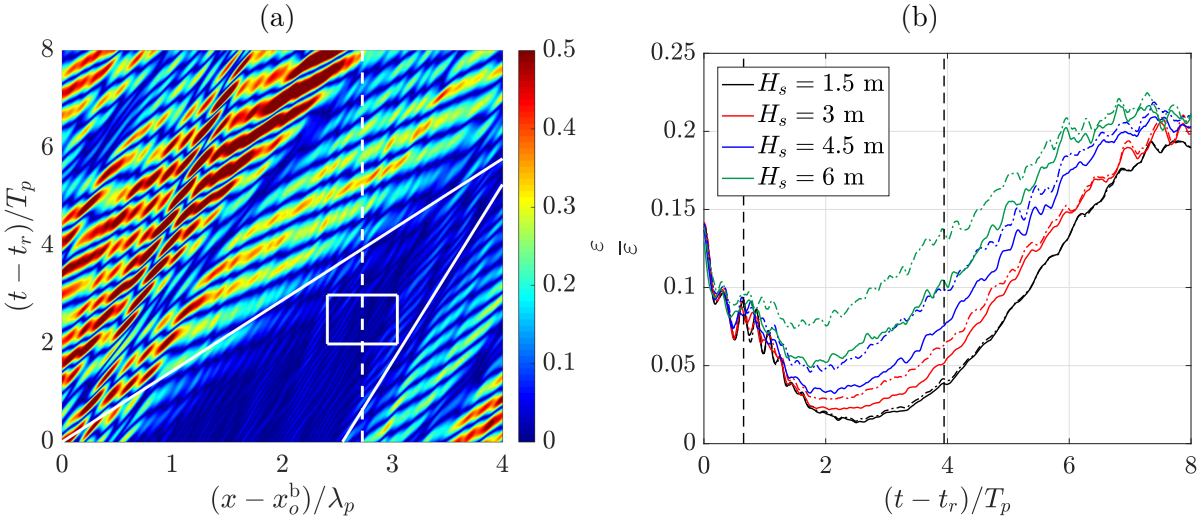

Figure 3: Numerical error of ocean reconstruction: (a) $\varepsilon(x,t)$ using ICWM for one realization with $H_s = 3$ m; white box marks the spatio-temporal target zone $\mathcal{T}(t)$, within the prediction zone $\mathcal{P}(t)$ marked by oblique lines; dashed line at $x = x_c$ marks sensor location. (b) $\bar{\varepsilon}$ (averaged over 1,000 realizations) at $x = x_c$, as a function of time, for different steepness using LWT (—·—·) or ICWM (———); vertical dashed lines mark the prediction zone boundaries.

according to Eq. (1) and group velocities $c_{g1,2}$, based on Eq. (4) for $k_{1,2}$, with $\mu = 5\%$. For this realization, the reconstruction error is very low in the spatio-temporal target zone $\mathcal{T}(t)$, within the prediction zone $\mathcal{P}(t)$. Note that the error is higher at $t = t_r$ for low x-values than in the rest of the prediction zone. This is due to the poor spatial sampling in this region which restricts high-frequency resolution. Since the badly resolved high-frequency components propagate slower than the rest of the wave components, they progressively leave the prediction zone as time increases. Figure 3b shows the time evolution of the same error averaged over 1,000 realizations at the sensor location x_c, for 4 different characteristic steepnesses (i.e., significant wave heights), using LWT or the ICWM model. For each steepness, the error decreases from a relatively large value at $t = t_r$, as waves enter the prediction zone (located between the vertical dashed lines in the figure) where it reaches its lowest value, and then increases to reach $\simeq 0.2$ after $8T_p$ of propagation. Within the prediction zone, ICWM does reduce ε in all cases as compared to LWT, but most significantly for the largest steepness (i.e., non-linearity). Also, due to nonlinear phase shifts for steep waves, the location of the minimum error shifts towards lower times as steepness increases.

Figure 4a further quantifies the prediction algorithm performance over the target zone (box in Fig. 3a), by plotting the time evolution of $\varepsilon_{\mathrm{RMS}}$ integrated within it, for LWT or the ICWM model. As observed earlier, this error significantly reduces using ICWM for average to high steepness. Moreover, $\varepsilon_{\mathrm{RMS}}$ only slowly varies with time and, hence, its time-average shown in Fig. 4b can provide a global estimate of the prediction model performance, as a function of the characteristic steepness H_s/λ_p. In all cases this average error reduces using ICWM rather than LWT, with the largest reduction, 13% (from 0.52 to 0.39), occurring for the steepest wave field. This confirms the importance of accurately representing nonlinear effects, with a model such as ICWM, when performing an ocean surface prediction based on observations, and in particular wave asymmetry and phase shifts, which increase as the sea state becomes more severe.

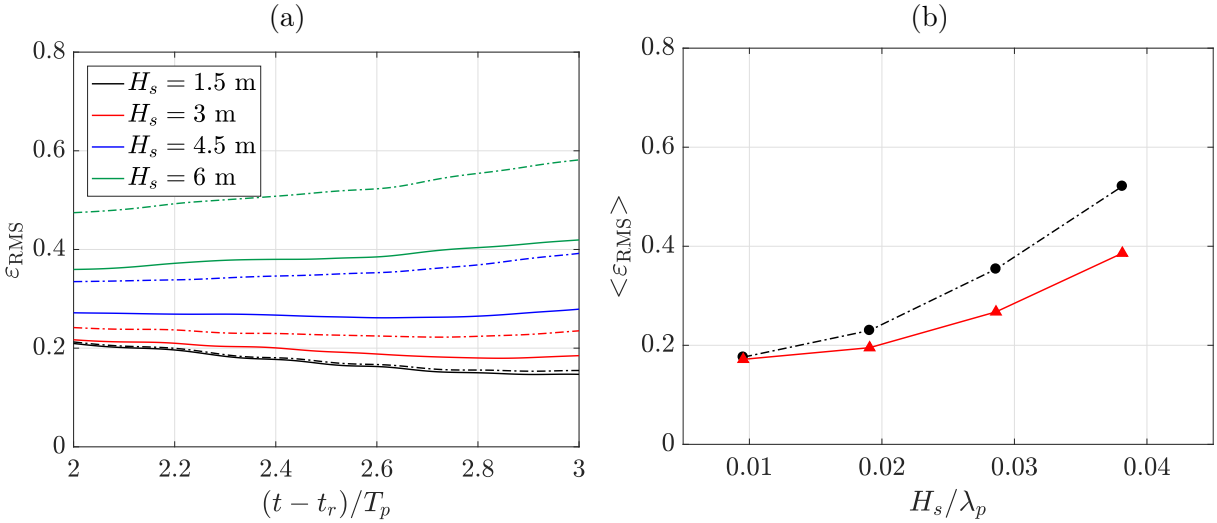

Figure 4: Numerical error of ocean reconstruction $\varepsilon_{\mathrm{RMS}}$: (a) Instantaneous; and (b) time-averaged over the target zone, for different steepnesses, using LWT (—·—·) or ICWM (———).

V – Experimental Data

Next, the prediction algorithm performance is assessed for an actual wave field using experimental data acquired in the ocean wave tank of École Centrale de Nantes (50 m × 30 m × 5 m).

V – 1 Experimental Setup

Laboratory experiments were performed in a wave tank, in which irregular waves were generated with a wavemaker, based on a full scale JONSWAP spectrum, with $T_p = 10$ s and $\gamma = 3.3$, and a few values of H_s (or characteristic wave steepness). Time series of surface elevation were measured using 20 fixed wave gauges, irregularly spaced according to a geometric law (neglecting wave shadowing effect; Fig. 5). Measurements made with these gauges are used as a proxy for

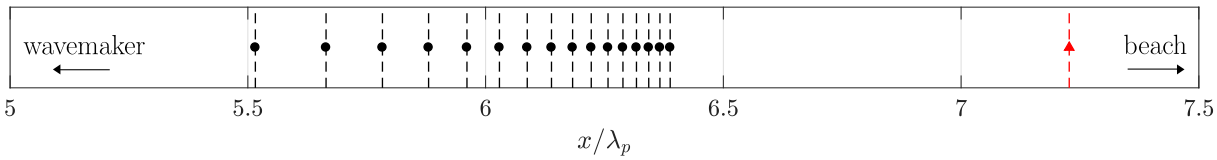

Figure 5: Locations of 16 (out of 20) irregularly spaced wave gauges (●) used in laboratory experiments; (▲) reference wave gauge.

data acquired at their location using an optical sensor. The equivalent optical sensor used in the model is located at an elevation $z_c = 20$ m, with a mean viewing angle $\alpha = 76°$, an aperture angle $\alpha_a = 20°$, $J = 20$ rays, and a $1/50^{\mathrm{th}}$ scale factor was used to account for wave tank limitations. In results reported here, only the first 16 probes are used, which are closest to the reference gauge (Fig. 5).

The number of observation times is set to $K = 100$, with a sampling frequency of 1.4 Hz, leading to an horizon of prediction $L_o = 2.78\lambda_p$, i.e., similar to that of the synthetic case (2.55). Unlike synthetic observations, only a finite and smaller number of independent realizations can be performed experimentally. However, an average can be made over dependent realizations by using a large enough time span between two reconstructions of the same wave field. Note that while convergence of result is slower using experimental data, statistical estimates can be approached with the method proposed by [14]. However, since the purpose of the experimental results presented here is only to illustrate the method using actual field data, such methods are not used here, but will be the object of future work.

V – 2 Results

Figure 6 shows time series of surface elevation for four different wave steepnesses, at the location of the reference probe (red triangle in Fig. 5). In the figure, t_1 corresponds to the first observation

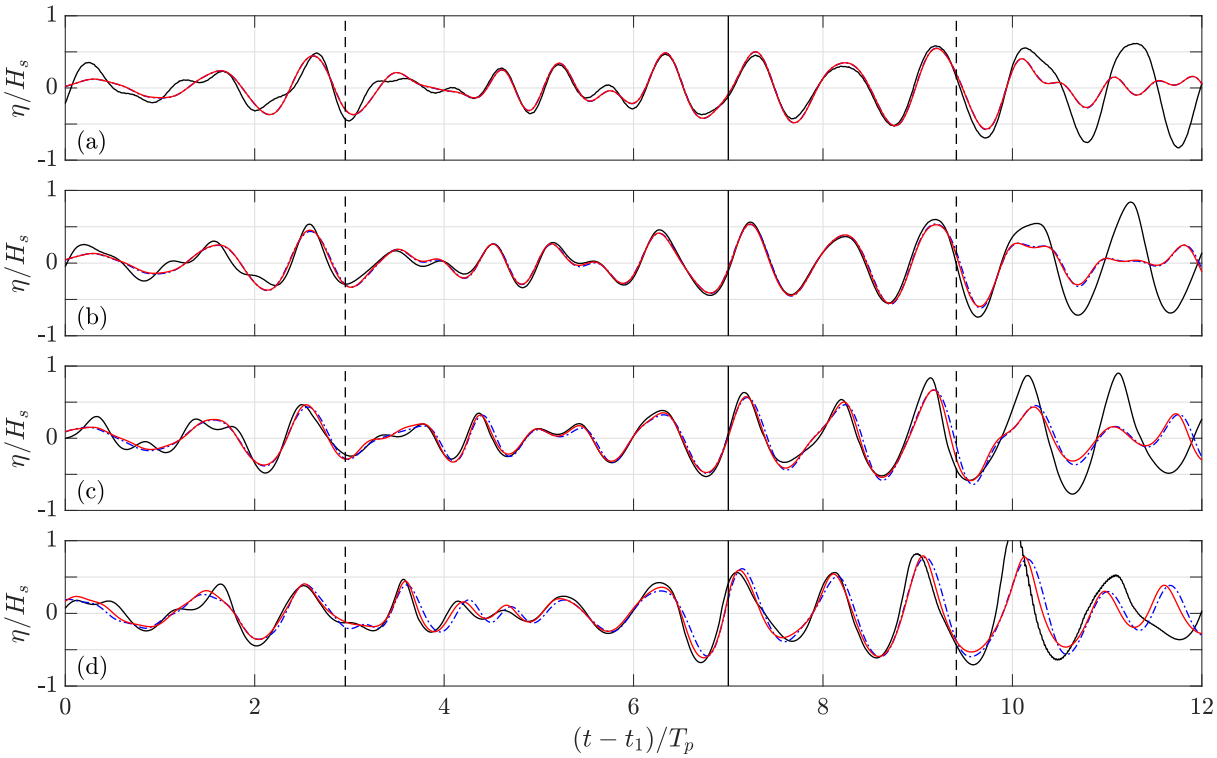

Figure 6: Time series of surface elevation in: (——) laboratory measurements, (–·–·–) LWT model, and (——) ICWM model, for H_s/λ_p = (a) 0.006, (b) 0.018, (c) 0.029 and (d) 0.041. Vertical continuous line corresponds to the reconstruction time t_r, and vertical dashed lines are boundaries of the prediction zone.

time. We see that the reconstruction time t_r is inside the prediction zone boundaries (calculated the same way to the synthetic case), which means that the assimilation time ($T_a = t_r - t_1 \simeq 7T_p$) is longer than the time needed by the information traveling at the slowest group velocity c_{g2} to reach the reference wave probe ($\simeq 3T_p$). Accordingly, the accessible prediction zone is divided in two parts, the forecast region $\mathcal{P}(t > t_r)$ and the hindcast region $\mathcal{P}(t < t_r)$. Surface elevations reconstructed/predicted by the LWT and the ICWM models are shown, and compared to the laboratory measurements. As expected, the prediction is close to measurements within the boundaries of the prediction zone. As the sea state characteristic steepness increases, the ICWM solution increasingly differs from the LWT solution, while being closer to the measured surface. Comparing the local surface shapes in the largest steepness case, one clearly sees that nonlinear wave properties are better accounted for when using the ICWM model. In particular, both the amplitude and phase of the steepest waves are better predicted.

VI – Conclusions

The characterization of the proposed ocean surface reconstruction and prediction algorithm, based on spatio-temporal optical measurements of surface elevation, was extended through the investigation of the influence of wave steepness on the prediction performance. For both synthetic and field data sets, wave prediction was significantly improved using the new ICWM model, as compared to LWT model, for moderate and high steepness. Results using synthetic or experimental data both show that nonlinear wave properties modeled by ICWM, such as wave shape asymmetry and phase shifts, are important for short-term ocean surface predictions.

Future efforts will include a comprehensive experimental validation of the presented algorithm, which will further assess the performance of the ICWM model for a directional wave field prediction.

Acknowledgment

This work is supported by Naval Group and Centrale Nantes through their Joint Laboratory for Marine Technology, and by the PREDEMO-NAV project, grant ANR-15-ASTR-0006.
F. Bonnefoy is gratefully acknowledged for substantial support on the experimental part of this work.

References

[1] E. Blondel, F. Bonnefoy, and P. Ferrant. Deterministic non-linear wave prediction using probe data. *Ocean Engineering*, 37:913–926, 2010.

[2] F. Bonnefoy, G. Ducrozet, D. Le Touzé, and P. Ferrant. *Advances in Numerical Simulation of Nonlinear Water Waves*, volume 11 of *Advances in Coastal and Ocean Engineering*, Chap. Time-Domain Simulation of Nonlinear Water Waves Using Spectral Methods, pages 129–164. World Scientific, 2009.

[3] D. Calvetti, L. Reichel, and A. Shuibi. L-curve and curvature bounds for tikhonov regularization. *Numerial Algorithms*, 35:301–314, 2004.

[4] H. Dankert, J. Horstmann, and W. Rosenthal. Wind- and wave-field measurements using marine x-band radar-image sequences. *IEEE Journal of Oceanic Engineering*, 30(3):534–542, July 2005.

[5] N. Desmars, Y. Perignon, G. Ducrozet, C.-A. Guérin, S. T. Grilli, and P. Ferrant. Phase-resolved reconstruction algorithm and deterministic prediction of nonlinear ocean waves from spatio-temporal optical measurements. In *ASME 2018 37th International Conference on Ocean, Offshore and Arctic Engineering*. American Society of Mechanical Engineers, 2018.

[6] G. Ducrozet, F. Bonnefoy, D. Le Touzé, and P. Ferrant. 3-d hos simulations of extreme waves in open seas. *Natural Hazards and Earth System Sciences*, 7:109–122, 2007.

[7] G. Ducrozet, F. Bonnefoy, D. Le Touzé, and P. Ferrant. Hos-ocean: Open-source solver for nonlinear waves in open ocean based on high-order spectral method. *Computer Physics Communications*, 203:245–254, June 2016.

[8] S. H. Gjosund. A lagrangian model for irregular waves and wave kinematics. *Journal of Offshore Mechanics and Arctic Engineering*, 125:94–102, May 2003.

[9] S. T. Grilli, C.-A. Guérin, and B. Goldstein. Ocean wave reconstruction algorithms based on spatio-temporal data acquired by a flash lidar camera. In *Proceedings of the Twenty-first International Offshore and Polar Engineering Conference (ISOPE2011)*, pages 275–282. International Society of Offshore and Polar Engineers, June 2011.

[10] C. Guérin, N. Desmars, S. Grilli, G. Ducrozet, Y. Perignon, and P. Ferrant. An improved lagrangian model for the time evolution of nonlinear surface waves. Under review for publication in Journal of Fluid Mechanics.

[11] P. C. Hansen, editor. *Computational inverse problems in electrocardiology*, Chap. The L-curve and Its Use in the Numerical Treatment of Inverse Problems, pages 119–142. WIT Press, p. r. johnston edition, 2001.

[12] T. Hilmer and E. Thornhill. Deterministic wave predictions from the wamos ii. In *OCEANS 2014 - TAIPEI*, pages 1–8, 2014.

[13] P. Naaijen, K. V. Oosten, K. Roozen, and R. V. Veer. Validation of a deterministic wave and ship motion prediction system. In *ASME 2018 37th International Conference on Ocean, Offshore and Arctic Engineering*. American Society of Mechanical Engineers, 2018.

[14] P. Naaijen, K. Trulsen, and E. Blondel-Couprie. Limits to the extent of the spatio-temporal domain for deterministic wave prediction. *International Shipbuilding Progress*, 61(3-4):203–223, 2014.

[15] F. Nouguier, B. Chapron, and C.-A. Guérin. Second-order lagrangian description of tri-dimensional gravity wave interactions. *Journal of Fluid Mechanics*, 772:165–195, June 2015.

[16] F. Nouguier, S. T. Grilli, and C.-A. Guérin. Nonlinear ocean wave reconstruction algorithms based on spatiotemporal data acquired by a flash lidar camera. *IEEE Transactions on Geoscience and Remote Sensing*, 52(3):1761–1771, March 2014.

[17] F. Nouguier, C.-A. Guérin, and B. Chapron. "choppy wave" model for nonlinear gravity waves. *Journal of Geophysical Research*, 114:1–16, September 2009.

[18] F. Nouguier, C.-A. Guérin, and B. Chapron. Scattering from nonlinear gravity waves: the "choppy wave" model. *IEEE Transactions on Geoscience and Remote Sensing*, 48(12):4184–4192, December 2010.

[19] W. J. Pierson. Models of random seas based on the lagrangian equations of motion. Technical report, New York University, April 1961.

[20] W. J. Pierson. Perturbation analysis of the navier-stokes equations in lagrangian form with selected linear solutions. *Journal of Geophysical Research*, 67(8):3151–3160, July 1962.

[21] Y. Qi, G. Wu, Y. Liu, and D. K. P. Yue. Predictable zone for phase-resolved reconstruction and forecast of irregular waves. *Wave Motion*, 2017.

[22] Y. Qi, W. Xiao, and D. K. P. Yue. Phase-resolved wave field simulation calibration of sea surface reconstruction using noncoherent marine radar. *Journal of Atmospheric and Ocean Technology*, 33:1135–1149, 2016.

[23] A. Simanesew, K. Trulsen, H. E. Krogstad, and J. C. N. Borge. Surface wave predictions in weakly nonlinear directional seas. *Applied Ocean Research*, 65:79–89, March 2017.

[24] K. Takagi, S. Hamamichi, R. Wada, and Y. Sakurai. Prediction of wave time-history using multipoint measurements. *Ocean Engineering*, 140:412–418, 2017.

[25] G. Wu. *Direct Simulation and Deterministic Prediction of Large-scale Nonlinear Ocean Wave-field*. PhD Thesis, Massachusetts Institute of Technology, May 2004.

[26] W. Xiao, Y. Liu, and D. K. P. Yue. Large-scale deterministic predictions of nonlinear ocean wave-fields. In *DoD High Performance Computing Modernization Program Users Group Conference*, pages 317–324, 2010.